Supplementary Information (SI) for Journal of Materials Chemistry A.

Supporting Information

Hydronium-Catching Interface Unlocks Strongly Acidic Zn Metal Batteries with High Voltage and Long-Term Stability

Zi-Fan He*,[1,2,3,+], Ting-Yu Wang[1,+], Ai Ling Huang[1], Chi-Yu Lai[1], Yi-Cheng Liao[1], Shafna Kunnathumpeedika[1], Chi-Chang Hu*,[1,4,5]

[1]Department of Chemical Engineering, National Tsing Hua University, Hsinchu 300044, Taiwan

[2]Thin Film PV Technology, Imec, Imo-imomec, Thor Park 8320, Genk 3600, Belgium

[3]Energy Ville, Imo-imomec, Thor Park 8320, Genk 3600, Belgium

[4]College of Semiconductor Research, National Tsing Hua University, Hsinchu 300044, Taiwan

[5]College of Sustainability, National Tsing Hua University, Hsinchu 300044, Taiwan

[+]Contribute equally

**: Corresponding author: Zi-Fan He, email: he01@imec.be*

**: Corresponding author: Chi-Chang Hu, email: cchu@che.nthu.edu.tw*

The supporting information includes **27 Figures and 8 Tables**.

Experimental procedures

1. Preparation of defective MOF-801

Defective MOF-801 was synthesized according to a reported method with slight modifications.[1] Specifically, $ZrCl_4$ (350 mg) and fumaric acid (160 mg) were dissolved in deionized (DI) water (8 mL). To engineer the defect density, the amounts of formic acid introduced into the solution were controlled. For MOF-4 (MOF-801 with a low defect density), 4 mL formic acid was added, whereas for MOF-2 (MOF-801 with a high defect density), 2 mL formic acid was used. The mixture was then sonicated for 1 h and left at room temperature for 24 h. The resulting precipitates were collected by centrifugation at 10,000 rpm, washed several times with DI water and ethanol, and finally dried at 80°C to yield defective MOF-801 powders.

2. Preparation of MOF-coated Zn electrodes

To prepare the electrode slurry, the as-synthesized MOF powders (MOF-4 or MOF-2, 20 mg) were mixed with PVDF binder (5 mg) and dispersed in 200 μL N-methyl-2-pyrrolidone (NMP). The mixture was stirred at 2000 rpm for 45 min using a mechanical stirrer to ensure homogeneous dispersion. For electrode fabrication, the resulting slurry was drop-cast onto one side of a zinc foil (~100 μm in thickness) with the area coating mass of MOF equal to 4 mg cm^{-2}. The MOF-coated electrodes were then dried in an oven at 80 °C for 2 h. The resulting electrodes are denoted as MOF-4@Zn or MOF-2@Zn, depending on the MOF used.

3. Cell assembly and electrochemical measurements

CR2032-type coin cells were assembled using MOF-4@Zn, MOF-2@Zn, or bare Zn foils (thickness ≈ 100 μm) as electrodes. A glass fiber separator (Whatman, thickness = 0.26 mm) and 60 μL of electrolyte (1 M $ZnSO_4$ + 1 M H_2SO_4) were used in each cell, sealed under a pressure of 50 kg cm^{-2}. Zn||Cu cells were assembled similarly, with one Zn electrode replaced by a Cu foil.

Linear sweep voltammetry (LSV) and Tafel analyses were carried out using Zn as the working electrode and Cu as both counter and reference electrodes in 1 M H_2SO_4 (pH = 0) to exclude Zn^{2+} effects and isolate the hydrogen evolution reaction (HER). The potential was scanned at 1 mV s^{-1}. Electrochemical impedance spectroscopy (EIS) was performed on Zn||Zn symmetric cells in 1 M $ZnSO_4$ + 1 M H_2SO_4 over a frequency range of 100 kHz – 0.01 Hz with an AC amplitude of 10 mV at the open-circuit potential. Distribution of relaxation time (DRT) analysis was conducted using the pyDRTtools package.

The cation transference number (T^+) was determined from symmetric Zn||Zn cells using 1 M $ZnSO_4$ as the electrolyte to exclude proton conduction, based on the Bruce–Vincent method.[2,3] Polarization measurements were conducted at a current density of 1 mA cm^{-2} in 1 M $ZnSO_4$ + 1 M H_2SO_4; the plateau overpotential was defined as the potential difference between the initial unpolarized voltage and the cell voltage at 0.1 mAh cm^{-2}. Chronoamperometry (CA) tests were performed at −150 mV under the same electrolyte condition.

4. *Full-cell evaluations*

Zn-PbO_2 batteries were assembled using commercial PbO_2 electrode (1 cm^2, Coommee Industrial Co., LTD.) as the positive electrode, a negative electrode of either bare Zn or MOF-2@Zn (1 cm^2), and 1 M $ZnSO_4$ + 2 M H_2SO_4 as the electrolyte. All Zn-PbO_2 batteries were tested in 4.5-mL commercial cell containers (Coommee Industrial Co., LTD.). Charging was conducted at 4 mA cm^{-2} to 0.5 mAh cm^{-2}, followed by discharge at 10 mA cm^{-2} to a cut-off voltage of 2.2 V. Overpotentials were determined as the voltage difference between 0 and 0.1 mAh cm^{-2} during the first charge/discharge cycle. For a comparison purpose, commercial two-cell series-connected lead–acid batteries (Coommee Industrial Co., LTD.) with their original electrolyte were tested under identical conditions by charging at 4 mA cm^{-2} to a capacity of 0.5 mAh cm^{-2} and discharging at 10 mA cm^{-2} to the same capacity.

Acidic Zn-ion hybrid capacitors (ZIHCs) were assembled using a negative electrode of either bare Zn or MOF-2@Zn (1.13 cm^2), an activated carbon positive electrode (1.13 cm^2, ACS25, China Steel Chemical Corporation), and the 1 M $ZnSO_4$ + 1 M H_2SO_4 electrolyte. The activated carbon electrode was fabricated by drop-casting the slurry onto a stainless steel substrate with a mass loading of 1 mg cm^{-1}. The bare Zn ZIHCs were prepared under the same conditions but using 1 M $ZnSO_4$ electrolyte only.

ZMABs (Zn//MnO_2) were constructed using a negative electrode of either bare Zn or MOF-2@Zn (1.539 cm^2), a CO_2-activated carbon felt (1.13 cm^2, thickness = 2 mm, CeTech. Ltd) as the positive electrode, and the 1 M $ZnSO_4$ + 1 M $MnSO_4$ + 0.3 M H_2SO_4 electrolyte. These cells were charged at 30 mA cm^{-2} to 0.2 mAh cm^{-2} and discharged to 1.0 V at 2 mA cm^{-2}.

5. *Characterizations*

The porosity and specific surface area of defective MOF-801 were determined from the N_2 adsorption-desorption isotherms at 77 K using the Brunauer–Emmett–Teller (BET) method (ASAP 2020 analyzer, Micromeritics).[4] The pore size distributions and cumulative pore volumes were analyzed using the N_2-DFT model in MicroActive for ASAP 2020. Surface properties were evaluated via the contact angle measurements (FTA-100B, First Ten Ångstrom). The chemical structure was analyzed using Fourier-transform infrared spectroscopy (FTIR, Thermo Fisher Scientific, USA). Raman spectroscopy (Thermo Scientific DXR Raman Microscope, $\lambda = 532$ nm) was employed to investigate the solvation structure of zinc ions.

The 1 M $ZnSO_4$ + 1 M H_2SO_4 confined within the MOF-2 sample was prepared by taking out the electrodes in MOF-2@Zn symmetric cells after 10 cycles at 1 mA/1 mAh cm^{-2}. Morphological characteristics were examined using the field emission scanning electron microscopy (FESEM, Hitachi SU8010), and crystallographic information of Zn electrodes was obtained via the X-ray diffraction (XRD, D8 Advance A25, Bruker, Germany).

The texture coefficient (TC) for a specific crystallographic plane (hkl) is calculated according to the following equation:

$$TC_{(hkl)} = \frac{\frac{I_{(hkl)}}{I_{(hkl)}^{o}}}{\frac{1}{n}\sum_{i=1}^{n}\left(\frac{I_{(hkl)i}}{I_{(hkl)i}^{o}}\right)}$$

where $I_{(hkl)}$ is the measured XRD intensity of the (hkl) plane, $I_{(hkl)}^{0}$is the standard intensity from the reference powder diffraction file (JCPDS card No. 04-0831 for Zn), and n is the number of diffraction peaks considered.

To further highlight the preferred orientation of the Zn (002) plane, the relative texture coefficient (RTC) is defined as:

$$RTC_{(002)} = \frac{TC_{(002)}}{\sum TC_{(hkl)}}$$

A higher $RTC_{(002)}$ value indicates a stronger preferred orientation along the (002) direction.

6. *Computational methods*

All density functional theory (DFT) calculations were performed using the DMol^3 module in Materials Studio. For the electrostatic potential (ESP) analysis, geometry optimization of the MOF-2 structure was performed using the generalized gradient approximation (GGA) with the BLYP (Becke-Lee-Yang-Parr) functional. The MOF-2 model was constructed from the MOF-801 framework by removing four organic linkers, following a previous report.[5]

For the adsorption analysis, geometry optimizations and adsorption calculations were carried out using the generalized gradient approximation (GGA) with the PBE

(Perdew-Burke-Ernzerhof) functional. Cluster models based on Zr_2 units were constructed to represent the local coordination environments of pristine and defective MOF-801 nodes. The pristine model was fully coordinated with formate ligands, while the defective model incorporated terminal OH and H_2O groups to mimic missing-linker defects. It should be noted that these cluster models are designed to capture local coordination changes induced by the defect formation rather than to reproduce the exact formate/fumarate ratios observed experimentally.

Adsorption energies (E_{ads}) were calculated as:

$$E_{ads} = E_{MOF + H_3O^+} - E_{MOF} - E_{H_3O^+}$$

where $E_{MOF + H_3O^+}$, E_{MOF}, and $E_{H_3O^+}$ represent the total energies of the combined system, the isolated MOF cluster, and the isolated hydronium ion, respectively. The Hirshfeld charge analysis was performed to evaluate the charge redistribution upon adsorption.

7. *Calculation methodology*

The areal and specific capacities of the Zn electrode were estimated from the galvanostatic charge–discharge (GCD) profiles using the following equations:

$$C_A = \frac{\int_0^{\Delta t} I dt}{A}$$

where C_A (mAh cm^{-2}) and C_m (mAh g^{-1}) represent the areal capacities; I (mA) is the applied current; Δt (h) is the discharge time; A (cm^2) is the electrode area.

For the half-cells, the formula for calculating cumulative (plating) capacity is followed by I/A × T/2, where T is operation time (h).

The areal capacity of the full Zn-based cell was obtained in the same manner:

$$C_{cell} = \frac{\int_0^{\Delta t} I dt}{A}$$

where C_{cell} (mAh cm^{-2}) denotes the cell areal capacity, and other symbols have the same meaning as above.

For full-cell performance evaluation, two normalization methods were adopted due to the large excess of the Zn foil employed in this work:

(i) Mass-balanced configuration (N/P = 1.5):

The energy and power densities in **Figure 3B** and **Table S4** were calculated on the basis of the total mass of active materials on both positive and negative electrodes under an N/P (negative/positive capacity) ratio of 1.5. In this case, the negative electrode mass was estimated according to the required capacity to satisfy N/P = 1.5.

(ii) Capacity-limiting electrode normalization:

For **Fig. S11** and **Table S5**, the energy and power densities were calculated based on the active mass of the capacity-limiting electrode (either positive or negative electrodes, depending on the system), consistent with commonly reported literature values.

The energy density (E) and specific power density (P) were calculated as:

$$E = \frac{\int_{V_1}^{V_2} C_{cell} dV}{m}$$

$$P = \frac{E}{1000 * \Delta t}$$

where E (Wh kg^{-1}) is the specific energy density, V_1 (V) and V_2 (V) are the lower and upper cutoff voltages, and Δt (h) is the discharge time, and m (mg cm^{-2}) is the mass used for normalization.

For the mass-balanced configuration with N/P = 1.5, m represents the total mass of the active material on the positive electrode and the corresponding matched Zn mass on the negative electrode. For the capacity-limiting electrode normalization, m corresponds to the active mass of the capacity-limiting electrode.

The active material loadings were determined as follows:

- Zn–PbO_2 cell: The PbO_2 mass was estimated based on Faraday's law (see **Figure S19**).

- ZMAB (Zn–MnO_2) cell: Since there is no MnO_2 on electrode initially, we use the theoretical capacity as the maximum specific capacity. The MnO_2 mass was then estimated based on Faraday's law.
- ZIHC (Zn–activated carbon) cell: the activated carbon mass was determined from the actual loading of active material.

Figures and Tables

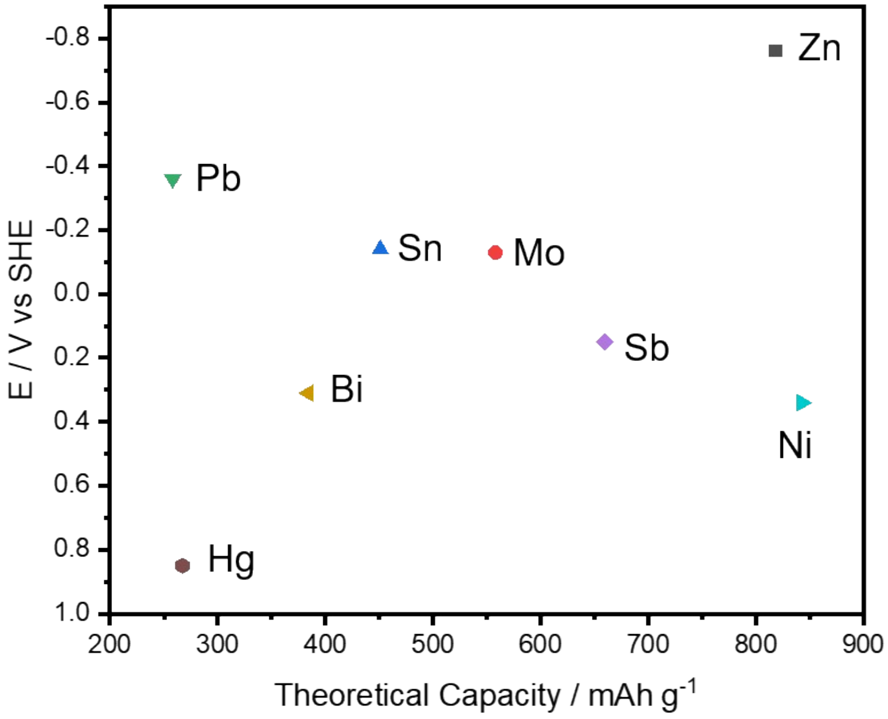

Figure S1. The comparison of Zn and other metals.

Among the metals stable in acidic environments, Zn stands out as the most promising anode material owing to its high theoretical capacity and relatively low redox potential. The Zn/Zn^{2+} redox couple provides a large electron transfer per unit mass, enabling high energy density, while its low potential maximizes the overall cell voltage and ensures good compatibility with a wide range of cathode materials. These advantages make Zn a superior anode candidate compared to other metals such as Mo, Sn, Pb, Sb, Bi, Cu, and Hg, whose corresponding redox reactions are shown below.

Zn: $Zn^{2+} + 2e^{-} \rightarrow Zn$

Mo: $Mo^{3+} + 3e^{-} \rightarrow Mo$

Sn: $Sn^{2+} + 2e^{-} \rightarrow Sn$

Pb: $PbSO_4 + 2e^{-} \rightarrow Pb + SO_4^{2-}$

Sb: $Sb_2O_3 + 6H^{+} + 6e^{-} \rightarrow 2Sb + 3H_2O$

Bi: $Bi^{3+} + 3e^{-} \rightarrow Bi$

Cu: $Cu^{2+} + 2e^{-} \rightarrow Cu$

Hg: $Hg^{2+} + 2e^{-} \rightarrow Hg$

1. *Defect chemistry and surface functionality of MOF-801*

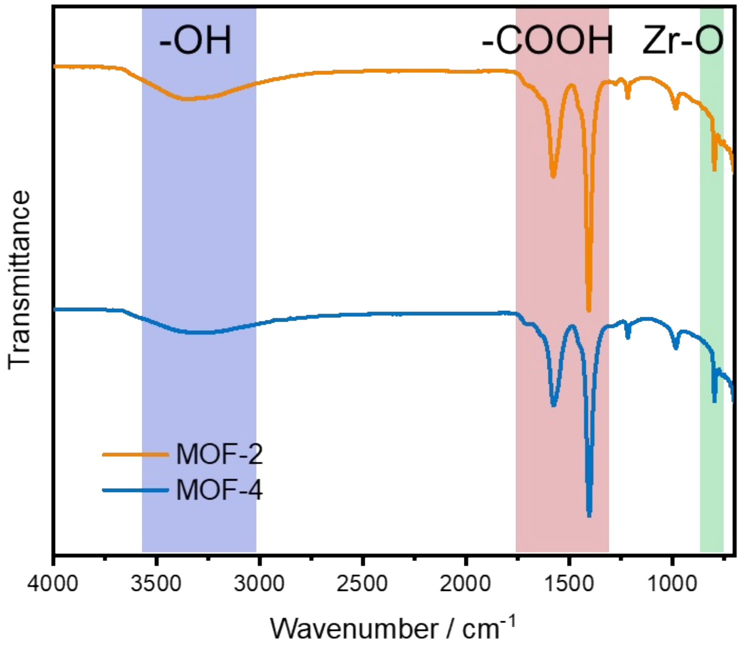

Figure S2. The FT-IR spectra of MOF-4 and MOF-2 powders.

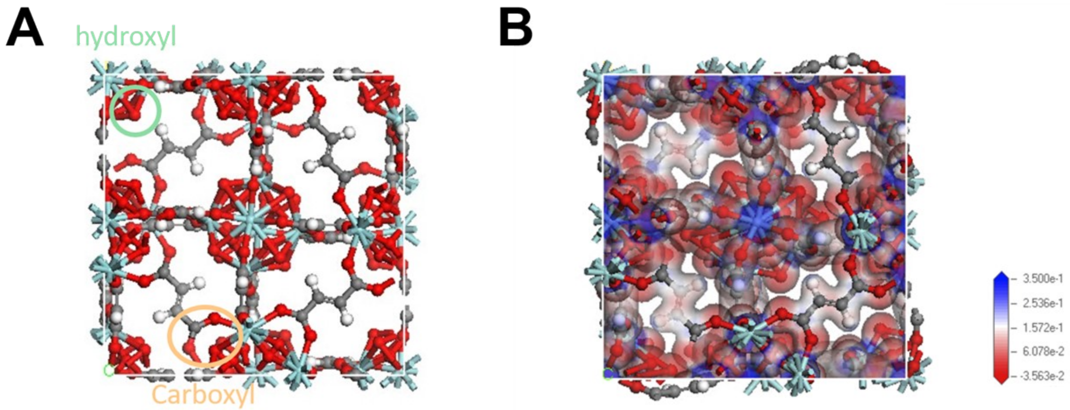

Figure S3. (A) The structure of MOF-2. (B) The electrostatic potential distribution of MOF-2.

MOF-2 was modeled by removing four linkers from the reference MOF-801 structure, resulting in the exposure of carboxyl and hydroxyl groups. The electrostatic potential distribution indicates that the most electronegative regions are centered around the oxygen atoms of these functional groups, highlighting their strong affinity for binding hydronium ions and water molecules.

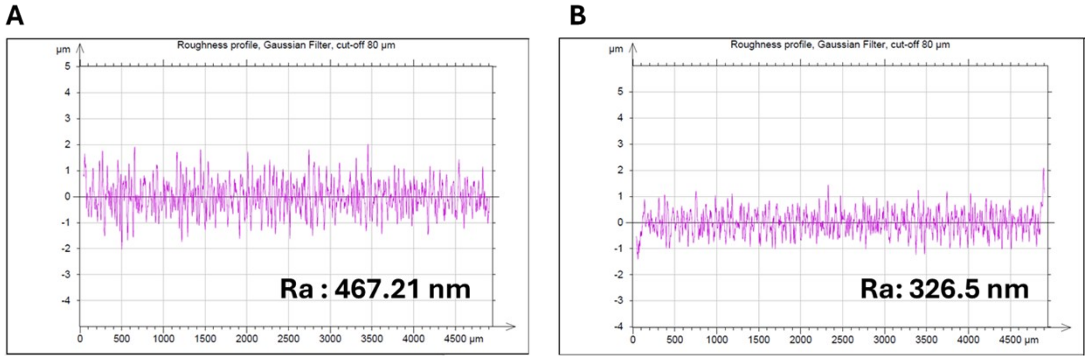

Figure S4. Linear surface roughness profiles of (A) MOF-2@Zn and (B) MOF-4@Zn measured by α-step over a scan length of 5000 µm.

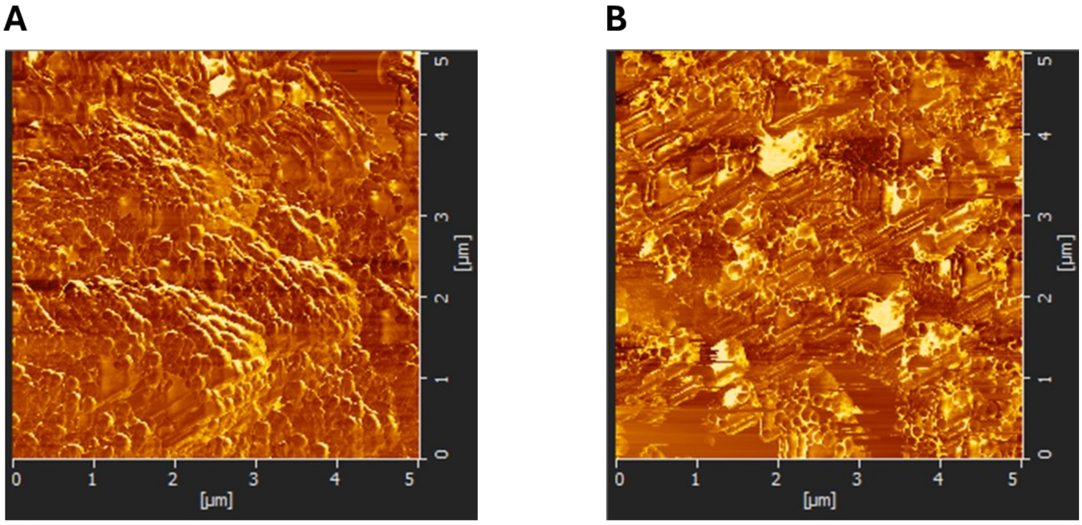

Sa	61.86nm
Sz/Smax	497.6nm

Sa	35.95nm
Sz/Smax	310.7nm

Figure S5. AFM topography images of (A) MOF-2@Zn and (B) MOF-4@Zn acquired over 5 × 5 μm^2 area.

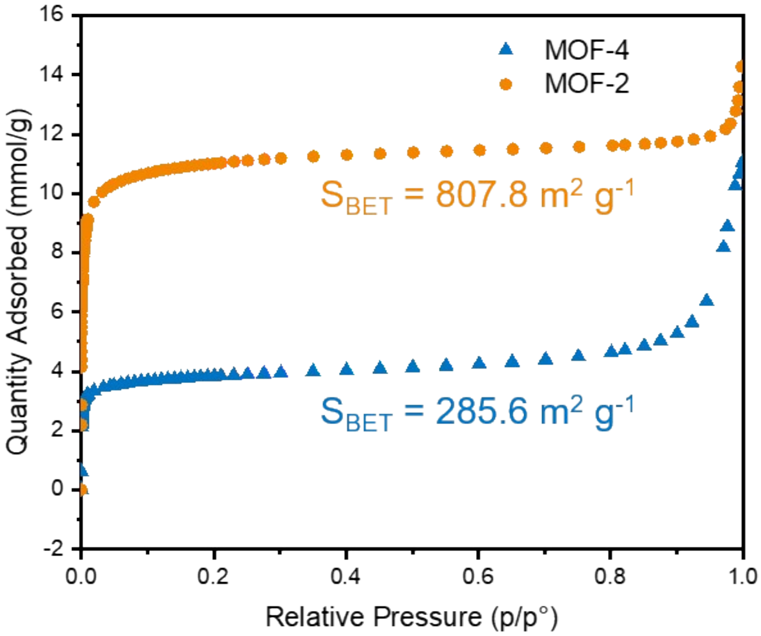

Figure S6. N_2 adsorption isotherms of MOF-4 and MOF-2. S_{BET} represents the surface area obtained from the isotherms.

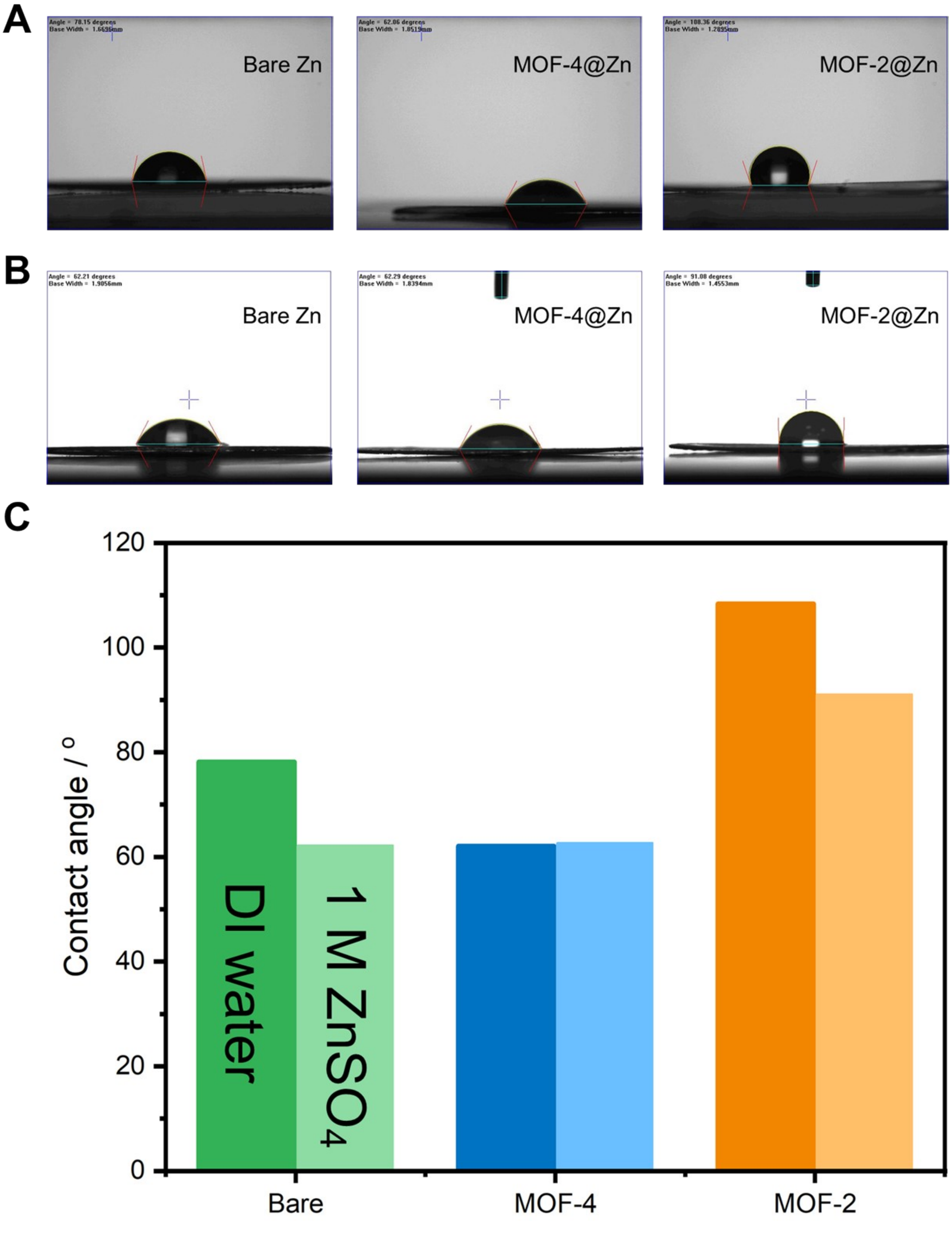

Figure S7. Contact angle images of (A) deionized water and (B) 1 M $ZnSO_4$ droplets on bare Zn, MOF-4@Zn, and MOF-2@Zn. (C) The summary of contact angle.

The wettability tests demonstrate the interfacial consequences of defect-related structural modifications. In deionized water, MOF-2@Zn exhibits a larger contact angle than MOF-4@Zn (**Figure S7A**), indicating a more hydrophobic external surface.

Yet in a 1 M $ZnSO_4$ solution (**Figure S7B**), the contact angles of both MOF-coated electrodes drop dramatically due to strong Zn^{2+} affinity, demonstrating their zincophilic nature. This hierarchical wettability, external hydrophobicity toward water but strong affinity toward Zn^{2+}, creates a selective transport regime where the bulk water ingress is minimized and the Zn^{2+} transport remains highly efficient, thereby preventing the uncontrolled hydronium accumulation at the metal surface.

Table S1. DFT total energies and adsorption energies for hydronium interaction with pristine and defect-modified MOF-801 cluster models.

Model	**E_{total} (Ha)**	**E_{H3O} (Ha)**	**E_{MOF} (Ha)**	**E_{ads} (Ha)**	**E_{ads} (kcal mol^{-1})**
Pristine	-8141.56	-76.6507	-8064.82	-0.08751	-54.9
Defect	-8028.86	-76.6507	-7952.09	-0.11755	-73.8

The calculated adsorption energies indicate that hydronium interacts more strongly with the defect-modified MOF-801 cluster than with the pristine model. The adsorption energy becomes more negative from −54.9 kcal mol^{-1} (pristine) to −73.8 kcal mol^{-1} (defect), corresponding to an enhanced stabilization of approximately 18.9 kcal mol^{-1} in the defect-modified local environment. This result suggests that the defect-induced coordination changes increase the affinity of the framework toward hydronium/proton species.

Table S2. Key structural parameters and Hirshfeld charge analysis for hydronium interacting with pristine and defect-modified MOF-801 models.

Model	**O–H$_1$ (Å)**	**O–H$_2$ (Å)**	**O–H$_3$ (Å)**	**H···O$_1$ (Å)**	**H···O$_2$ (Å)**	**H$_3$O charge**
Pristine	1.079	1.054	0.976	1.396	1.498	0.43
Defect	1.510	0.972	0.989	1.041	1.854	0.24
H_3O^+ (isolated)	0.992	0.992	0.992	–	–	–

Structural parameters further reveal the distinct differences in hydronium–framework interactions between the two models. In the defect-modified structure, one O–H bond in H_3O^+ is significantly elongated (1.510 Å) compared to the pristine model, accompanied by a markedly shorter H···O distance (1.041 Å) to a nearby oxygen site. This geometry indicates stronger proton sharing interactions in the defect-associated local environment. In contrast, the pristine model exhibits the less pronounced O–H elongation and longer hydrogen-bond distances, consistent with the weaker interactions.

The Hirshfeld charge analysis shows that the residual positive charge on hydronium decreases from 0.43 in the pristine model to 0.24 in the defect-modified model, indicating the enhanced charge redistribution between hydronium and the framework. These results collectively support the stronger hydronium/proton stabilization in the defect-modified local coordination environment. This enhanced stabilization is consistent with the proposed hydronium-regulated interfacial environment discussed in the main text.

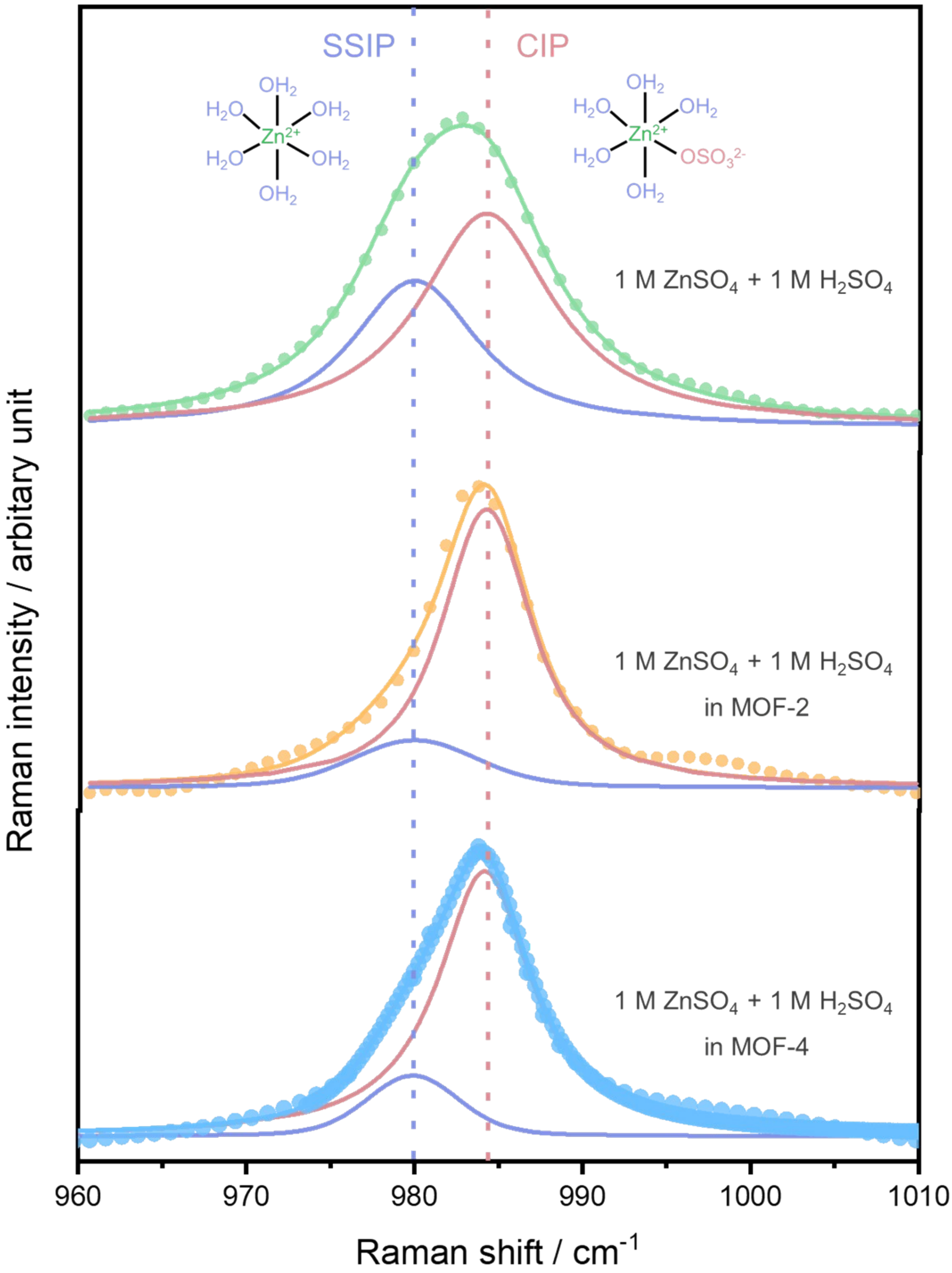

Figure S8. Deconvoluted v(SO_4^{2-}) bands revealing an increased fraction of contact ion pairs (CIPs) in MOF-confined electrolytes, consistent with a modified Zn^{2+} solvation structure induced by the reorganized IHL.

2. Performance of acidic Zn symmetric cells and full-cell systems

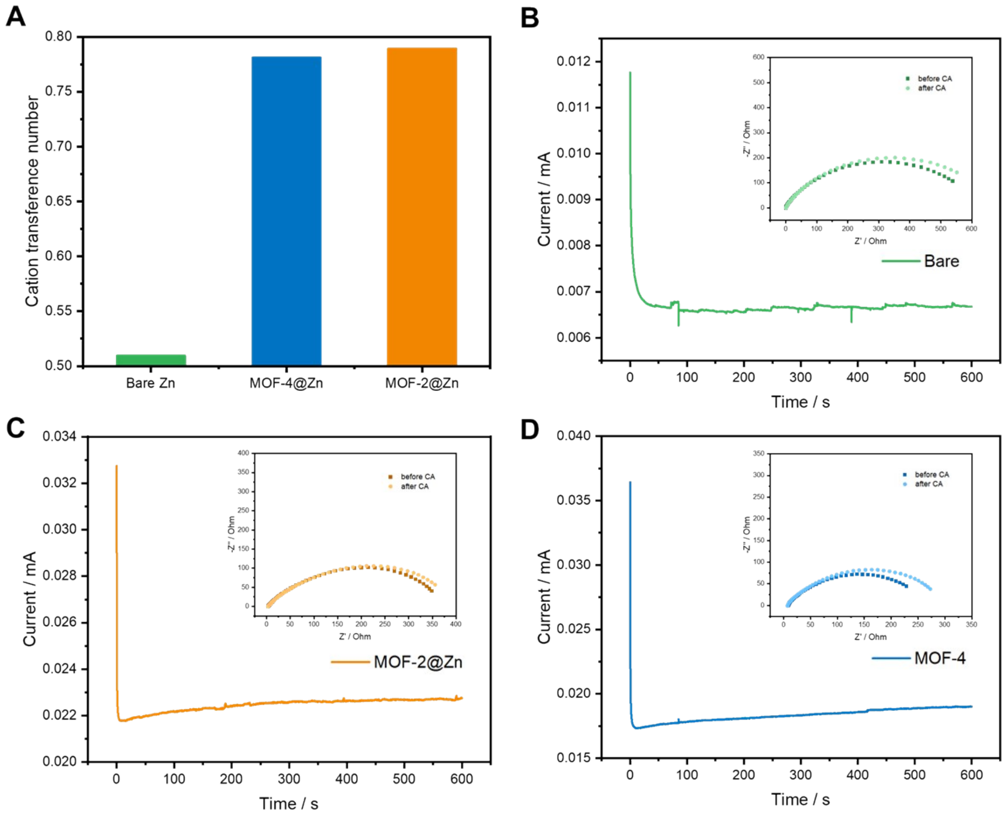

Figure S9. (A) Summary of cation transference numbers. EIS of the (B) bare Zn symmetric cell (C) MOF-2@Zn symmetric cell and (D) MOF-4@Zn symmetric cell before and after polarization. The current evolution during polarization at 10 mV is also shown. Fitting results are shown in **Table S3**.

Table S3. Fitting results of the EIS spectra in **Figure S9** using the specified equivalent circuit.

	Bare Zn		MOF-4@Zn		MOF-2@Zn	
	Before EIS	After EIS	Before EIS	After EIS	Before EIS	After EIS
R_S/Ohm	0.8472	1.27	8.51	7.298	3.362	3.355
Q_{INT}/Fs^{a-1}	3.50E-05	3.50E-05	7.03E-04	6.49E-04	7.95E-04	7.48E-04

a_{INT}	0.9045	0.8445	0.7409	0.754	0.587	0.593
R_{INT}/Ohm	55.65	98.4	52	46.7	149.2	146.1
Q_{PASS}/Fs^{a-1}	6.97E-05	5.97E-05	1.29E-03	1.14E-03	1.19E-03	1.23E-03
a_{PASS}	0.71	0.695	0.7303	0.7395	0.7206	0.732
R_{PASS}/Ohm	565	588.2	206.3	240	227.4	248.2

The electrochemical impedance spectroscopy (EIS) was conducted on the Zn symmetric cells using 1 M $ZnSO_4$ as the electrolyte to evaluate the cation transference number (T^+). H_2SO_4 was excluded from the electrolyte to avoid proton conduction, which would dominate the charge transport and obscure the intrinsic Zn^{2+} contribution to T^+.

EIS spectra were collected before and after a small polarization of 10 mV, with the corresponding current response shown in **Figure S9**. Spectra were fitted with an equivalent circuit comprising the solution resistance R_S in series with the passivation layer impedance (Z_{PASS}, passivation/SEI-like layer and contact effects) and the interfacial impedance (Z_{INT}, Zn plating/stripping-related kinetics); i.e., $Z_{TOTAL} = R_S + Z_{PASS} + Z_{INT}$ where Z_{PASS} was modeled as the passivation layer resistance (R_{PASS}) in parallel with a constant phase element (CPE_{PASS}) and Z_{INT} is modeled as an interfacial resistance (R_{INT}) in parallel with a constant phase element (CPE_{INT}). The presence of the interface impedance (Z_{PASS}) is attributed to the absence of H_2SO_4 in the electrolyte, favorable for the formation of a passive/SEI-like layer.

The cation transference number (T^+) was calculated using the Bruce–Vincent equation: $T^+ = \frac{I_{ss}(\Delta V - R_0 I_0)}{I_0(\Delta V - R_{ss} I_{ss})}$, where the ΔV is the voltage polarization applied (10 mV); I_0 and R_0 are initial current and overall interfacial resistance, respectively; I_{ss} and

R_{ss} denote the steady-state current and overall interfacial resistance, respectively. The overall interfacial resistance values of R_0 and R_{ss} were determined as the sum of R_{PASS} and R_{INT} extracted from the fitting results (**Table S3**).

The calculated T^+ values were 0.51, 0.78, and 0.79 for bare Zn, MOF-4@Zn, and MOF-2@Zn, respectively. The enhanced T^+ for MOF-coated electrodes confirms that the defect-rich MOF layers improve the Zn^{2+}-selective conduction across the electrode/electrolyte interface. In particular, MOF-2 achieves the highest T^+ and maintains the stable passivation resistance, demonstrating its superior ability to regulate the Zn^{2+} flux and suppress the side reactions.

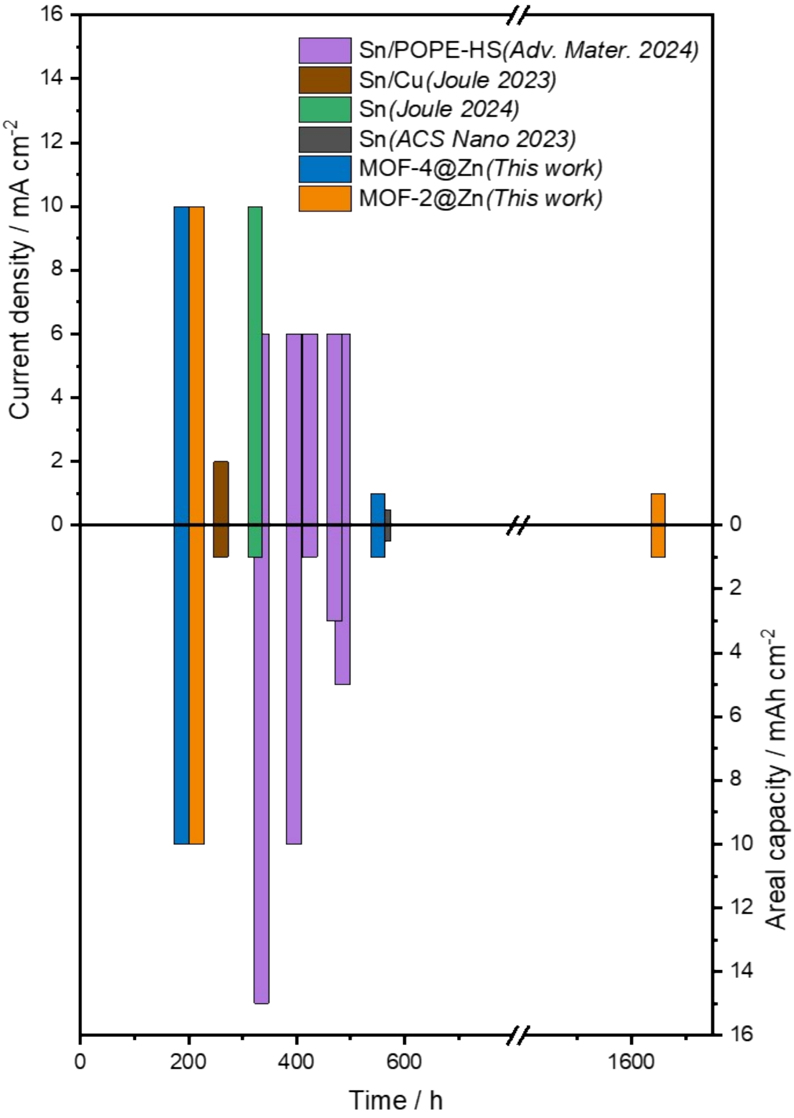

Figure S10. Performance comparisons of recently reported aqueous acidic metal symmetric cells.[6-9]

Table S4. Electrochemical performances of MOF-2@Zn AABs and recent reported AABs based on the total mass of active materials on both positive and negative electrodes. For the MOF-2@Zn systems, the performance parameters are calculated using a mass-balanced configuration with an N/P ratio of 1.5. As for the literature data, values reported based on total mass are directly adopted, while those lacking such normalization are estimated using the reported N/P ratios and electrode capacities.[7] Estimated values are shown in italics.

Battery	Voltage / V	Maximum specific capacity / mAh g^{-1}	Energy density /Wh kg^{-1}	Power density /kW kg^{-1}	Lifespan / cycles	Ref
CuFe-TBA//MoO_3	1.1	46	34.5	4	1000	[10]
p-chloranil/rGO//Pb	1.02	*115.6*	*117.9*	*0.1*	3000	[11]
Alizarin//Alizarin	1	81.5	81.5	2.2	100	[12]
PTC//PUQ	0.72	78.1	56.2	0.3	1000	[13]
pEP(QH2)E//pEP(NQ)E	0.4	*24.31*	*9.72*	*0.73*	500	[14]
InHCF//DPPZ	0.82	37	28	0.76	3000	[15]
PEDOT-BQ//PEDOT-AQ	0.5	40	20	0.023	150	[16]
MnO2@GF//PTO	0.85	183.9	132.6	0.0256	5000	[17]
MnO_2//Alloxazine	1.2	117.7	89	1.34	500	[18]
MnO_2//MoO_3	1.5/1.14	156.4	177.4	0.896	300	[19]
MnO_2//Sn	1.5	*255.1*	*312.2*	*6.8*	2400	[7]
MnO_2//MOF-2@Zn	**1.7**	**289.8**	**502.8**	**5.3**	**487**	**This work**
Ac//MOF-2@Zn	**1**	**58.6**	**59.3**	**0.9**	**30000**	**This work**
PbO_2//MoF-2@Zn	**2.35**	**12.0**	**28.5**	**8.8**	**117**	**This work**

Table S5. Electrochemical performances of MOF-2@Zn AABs and recent reported AABs based on the active mass of capacity-limiting electrodes. The unreported performance parameters were estimated by the reported data provided in the references including galvanostatic charge-discharge curves, mass loading of positive and negative electrodes, ideal N/P ratio with theoretical capacity when the electrode mass loadings were not given.[7] Estimated values are shown in italics.

Battery	Voltage / V	Maximum specific capacity / mAh g^{-1}	Energy density / Wh kg^{-1}	Power density / kW kg^{-1}	Lifespan / cycles	Ref
CuFe-TBA//MoO_3	1.1	*76.7*	*57.5*	*6.7*	1000	[10]
p-chloranil/rGO//Pb	1.02	208.0	*212.2*	*0.2*	3000	[11]
Alizarin//Alizarin	1	*163.0*	*163.0*	*4.4*	100	[12]
PTC//PUQ	0.72	*160.1*	*115.2*	*0.6*	1000	[13]
pEP(QH2)E//pEP(NQ)E	0.4	60.0	24.0	1.8	500	[14]
InHCF//DPPZ	0.82	*51.2*	*38.8*	*1.1*	3000	[15]
PEDOT-BQ//PEDOT-AQ	0.5	120.0	60.0	0.1	150	[16]
MnO2@GF//PTO	0.85	*616.5*	*444.5*	*0.1*	5000	[17]
MnO_2//Alloxazine	1.2	*616.5*	*466.2*	*7.0*	500	[18]
MnO_2//MoO_3	1.5/1.14	*616.5*	*699.3*	*3.5*	300	[19]
MnO_2//Sn	1.5	*617.3*	755.5	*16.5*	2400	[7]
MnO_2//MOF-2@Zn	**1.7**	**616.5**	**1069.8**	**11.3**	**487**	**This work**
Ac//MOF-2@Zn	**1**	**65.6**	**66.4**	**1.0**	**30000**	**This work**
PbO_2//MoF-2@Zn	**2.35**	**12.2**	**29.1**	**0.6**	**117**	**This work**

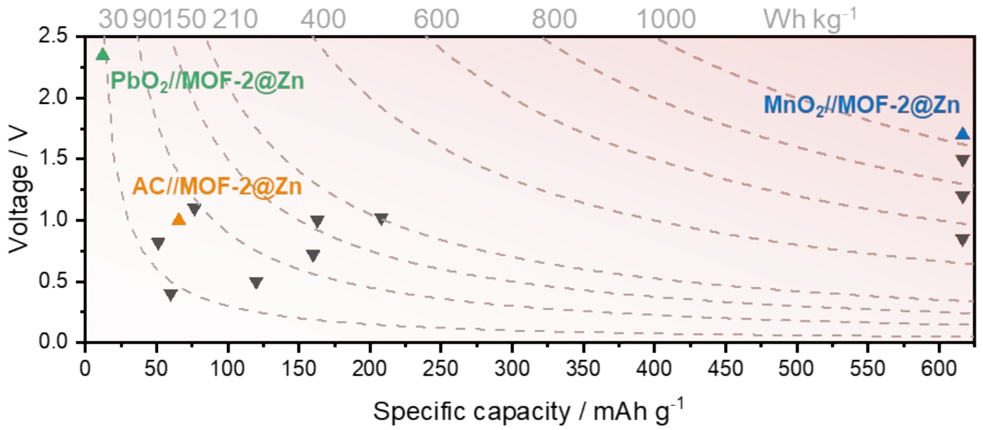

Figure S11. Performance comparisons of MOF-2@Zn AABs with recent reports, plotted against the active mass of capacity-limiting electrodes (**Table S5**).

Table S6. The calculated energy densities (Wh kg^{-1}) of MOF-2@Zn systems based on three normalization methods, including positive electrode mass, negative electrode mass (using excess Zn foil), and the combined mass of both electrodes. Values based on a mass-balanced configuration with an N/P ratio of 1.5 are also included for comparisons.

	Positive electrode mass	Negative electrode mass (Zn foil)	Total mass (Zn foil)	Total mass (N/P=1.5)
Zn//MnO_2	1069.8	4.5	4.5	502.8
Zn//AC	66.4	0.9	0.9	59.3
Zn//PbO_2	46.7	16.4	10.5	28.5

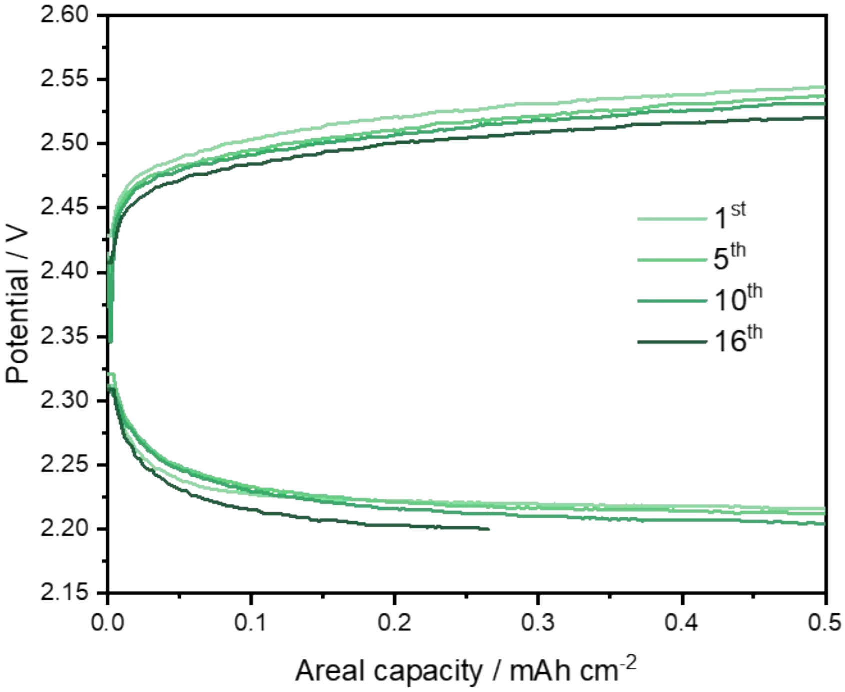

Figure S12. Charge/discharge profiles of the bare Zn-PbO$_2$ battery.

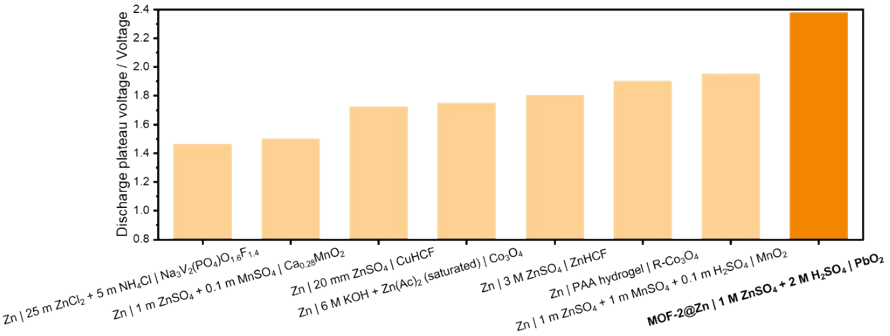

Figure S13. State-of-the-art of high-voltage Zn-based aqueous batteries.[20-26]

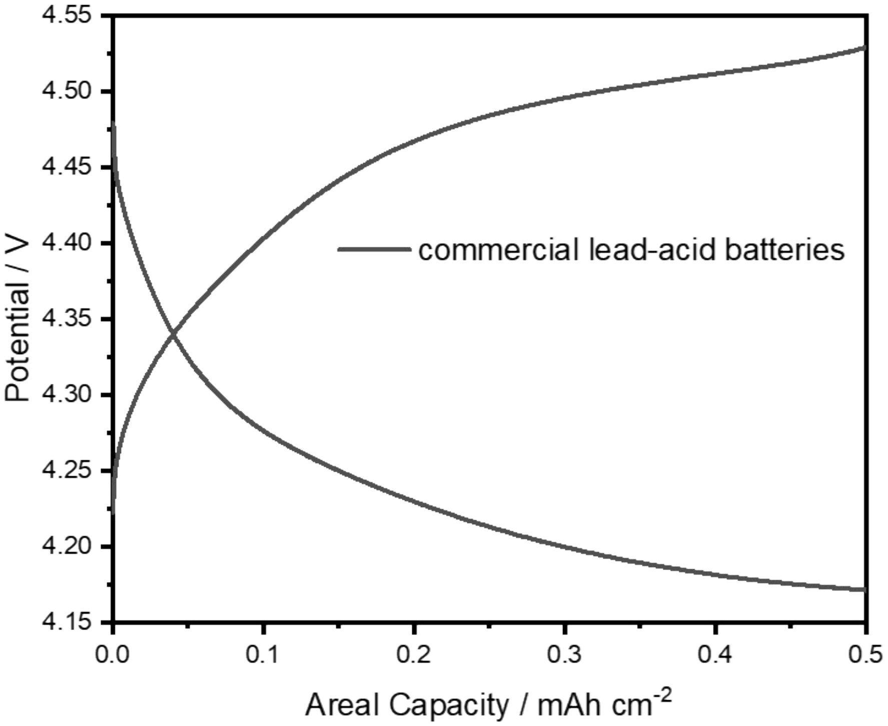

Figure S14. Charge/discharge profiles of the commercial lead-acid battery.

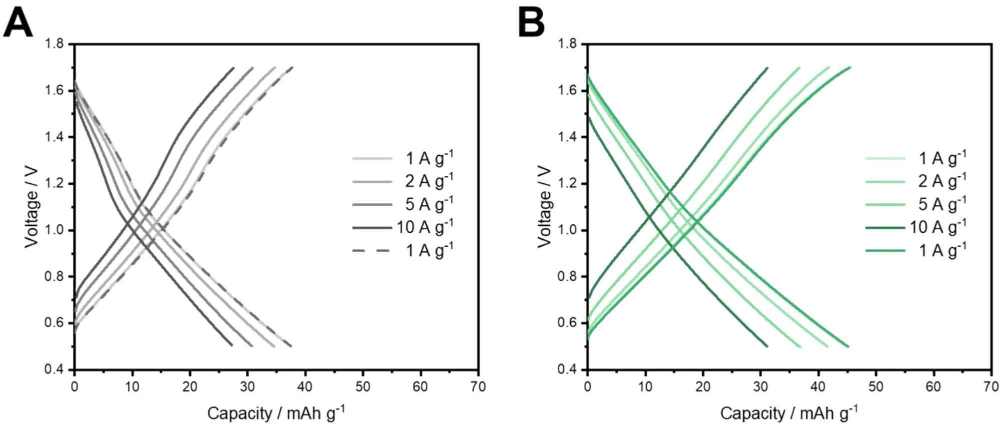

Figure S15. Charge/discharge profiles at various current densities of (A) the bare Zn ZIHC (1 M $ZnSO_4$) and (B) the bare Zn acidic ZIHC (1 M $ZnSO_4$).

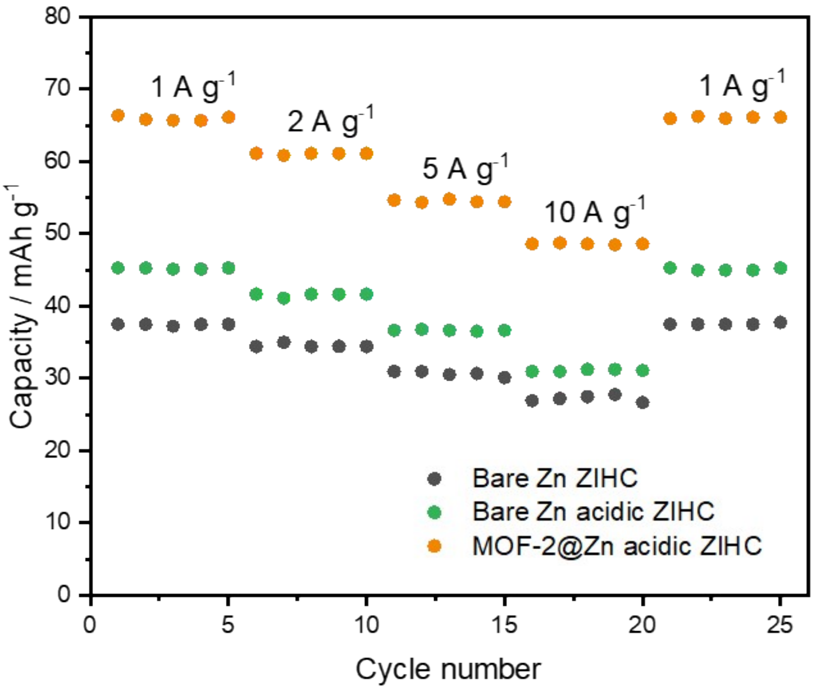

Figure S16. Rate performance of the bare Zn ZIHC, bare Zn acidic ZIHC, and MOF-2@Zn acidic ZIHC at 10 A g^{-1}.

To further evaluate the capacitive behavior of the Zn-ion hybrid capacitors (ZIHCs), charge–discharge profiles of bare Zn ZIHCs with and without H_2SO_4 were compared

(**Figure S15**). Here, ZIHCs were assembled using either bare Zn or MOF-2@Zn as the negative electrode, and commercially available activated carbon (AC) as the positive electrode. The two acidic ZIHCs employed 1 M $ZnSO_4$ + 1 M H_2SO_4 as the electrolyte, while the bare Zn ZIHC utilized 1 M $ZnSO_4$ alone. The addition of 1 M H_2SO_4 significantly enhances the ionic conductivity of the electrolyte, thereby reducing the internal resistance and accelerating the charge transport.[27,28] As a result, the bare Zn acidic ZIHC delivers higher discharge capacities than the neutral ZIHC across all current densities, owing to the additional proton participation in the charge storage process.[29] However, in the absence of the MOF-2 protection layer, the bare Zn acidic ZIHC suffers from approximately 35% capacity decay after extended cycling, which can be attributed to parasitic hydrogen evolution and corrosion at the Zn interface.

As shown in **Figure S16**, the rate performance comparison among the bare Zn ZIHC, bare Zn acidic ZIHC, and MOF-2@Zn acidic ZIHC further highlights the effectiveness of the MOF coating. The MOF-2@Zn device exhibits markedly higher discharge capacities and superior rate stability at all current densities. These results confirm that the hydronium-catcher interface of MOF-2 not only stabilizes Zn in highly acidic environments but also ensures fast ion transport and efficient capacitive energy storage.

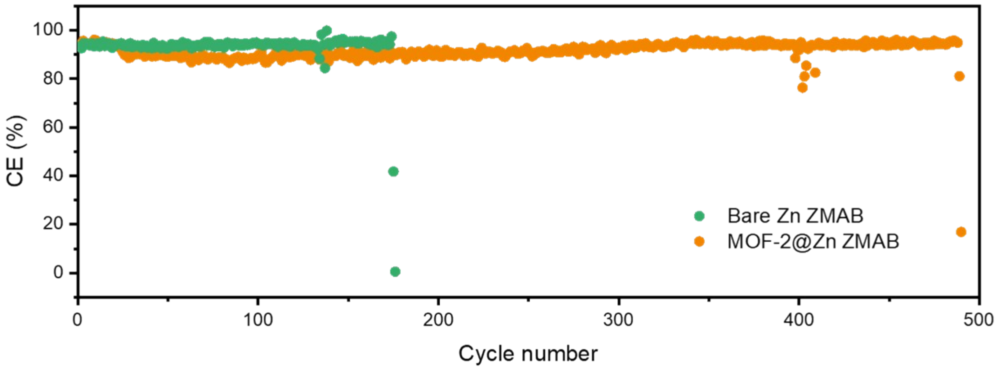

Figure S17. Cycling performances of the bare Zn ZMAB and MOF-2@Zn ZMAB.

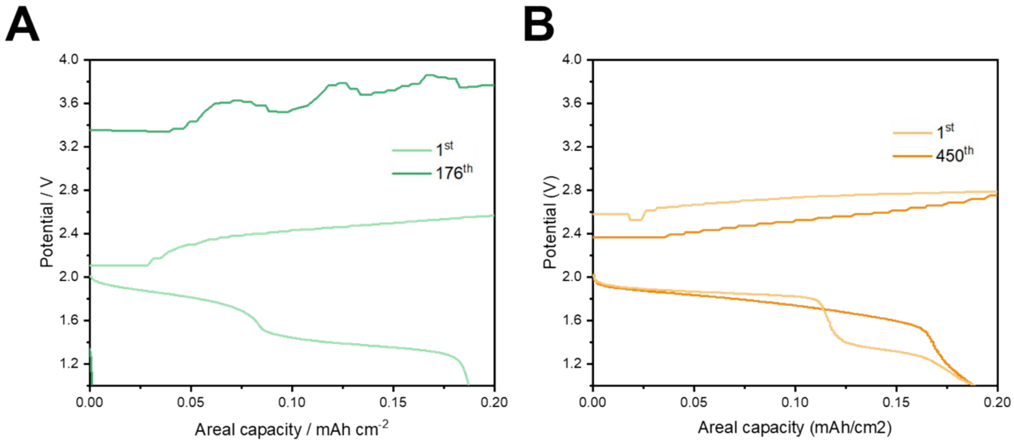

Figure S18. Charge-discharge profiles of (A) the bare Zn ZMAB and (B) the MOF-2@Zn ZMAB.

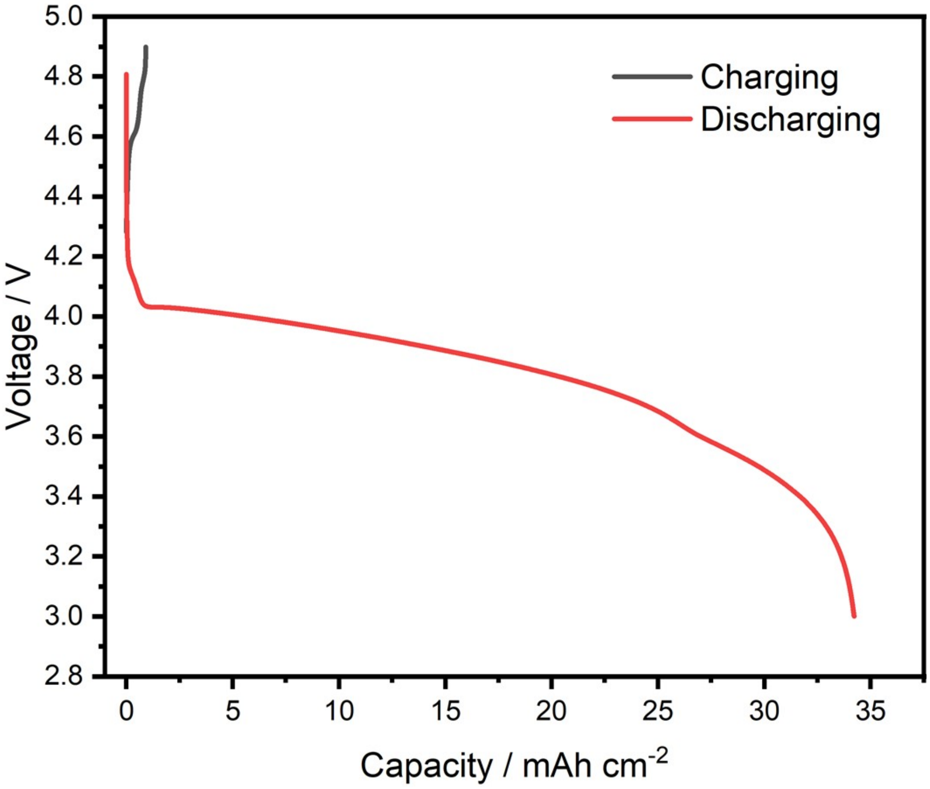

Figure S19. Complete discharge test of a commercial lead–acid battery.

To estimate the active mass of the PbO_2 positive electrode, a commercial lead–acid battery was tested without any preconditioning. The cell was first charged at 3.75 mA cm^{-2} to ensure the electrode reached a fully oxidized state and to exclude the contribution of any residual reactants. As shown in **Figure S19**, the charging capacity was approximately 0.9 mAh cm^{-2}, showing no distinct plateau, indicating that the electrode was already in a nearly fully charged condition. The subsequent discharge at 12.5 mA cm^{-2} delivered a total capacity of 34.2 mAh cm^{-2}.

According to Faraday's law, this corresponds to an active mass of approximately 40.9 mg cm^{-2} of PbO_2 (reaction: $PbO_2 + 4H^+ + 2e^- \rightarrow Pb^{2+} + 2H_2O$). The electrode was also weighed before and after the charge–discharge process, yielding a mass difference of 39.8 mg cm^{-2}, which is in excellent agreement with the theoretical estimation.

It should be noted that this experiment represents a full discharge to nearly 100 %

depth of discharge (DoD) for the purpose of active mass estimation; in practical lead–acid batteries, such deep discharge is typically avoided to prevent electrode degradation.

3. Temperature-dependent interfacial kinetics and DRT analysis

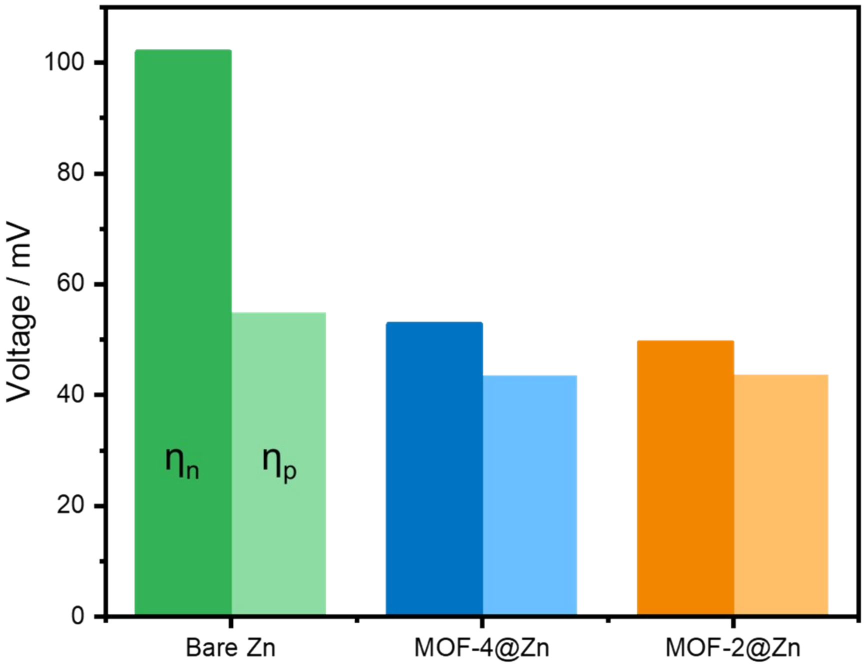

Figure S20. Summary of nucleation (η_n) and quasi-steady-state deposition (η_p) overpotentials of bare Zn, MOF-4@Zn, and MOF-2@Zn symmetric cells.

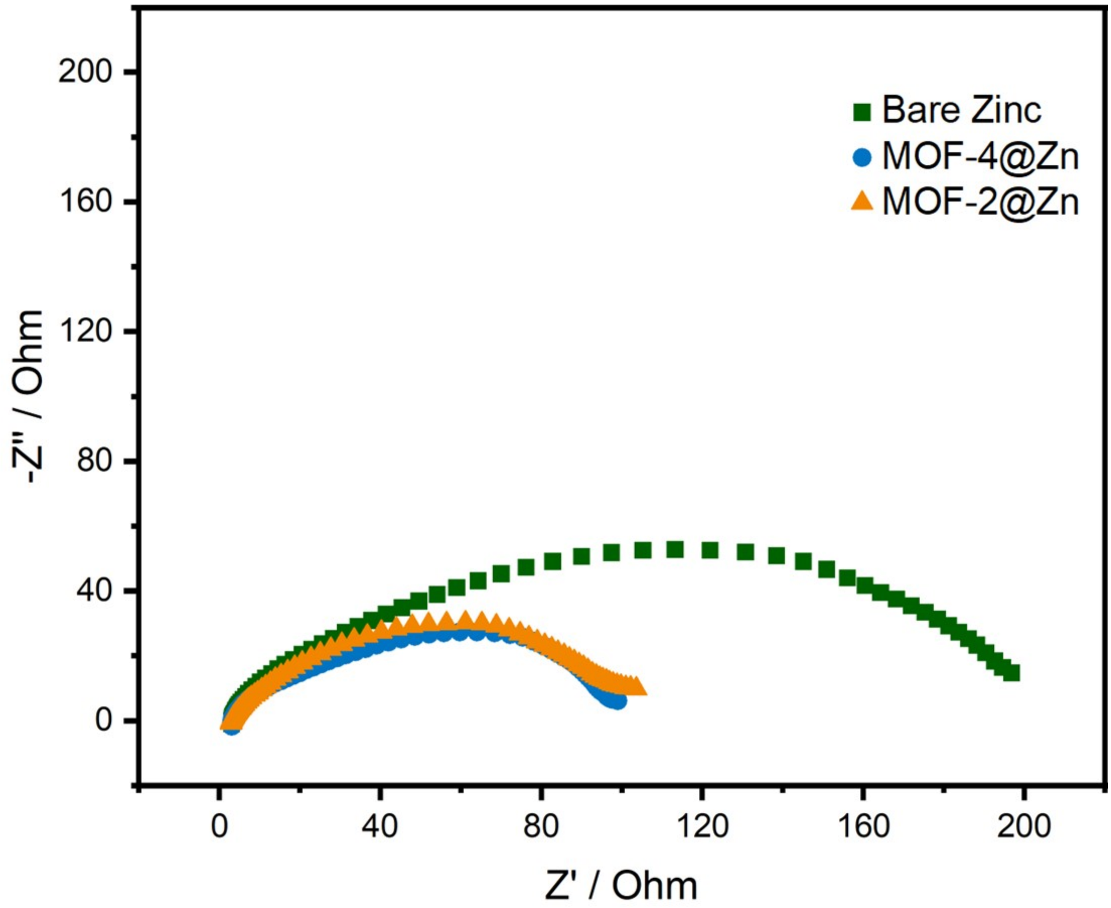

Figure S21. (C) Nyquist plots of bare Zn, MOF-4@Zn, and MOF-2@Zn symmetric cells.

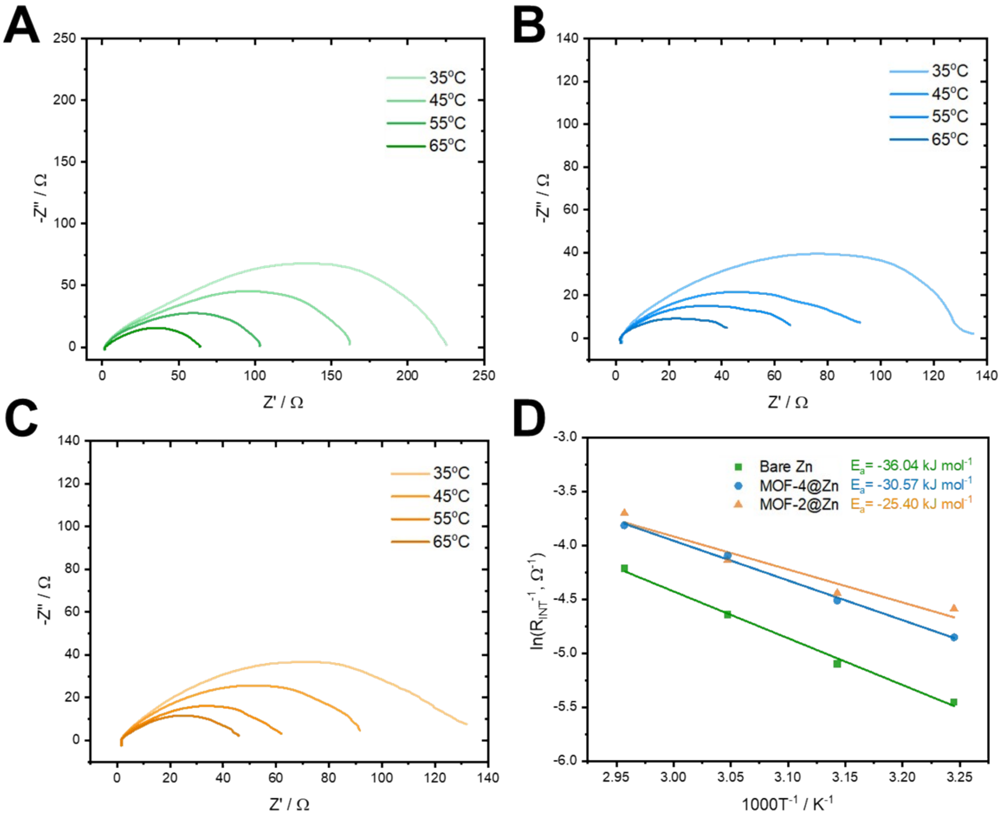

Figure S22. Nyquist plots of (A) bare Zn, (B) MOF-4@Zn, and (C) MOF-2@Zn at 35, 45, 55, and 65°C. Fitting results are shown in **Table S7**.

Table S7. Fitting results of the EIS spectra in **Figure S22** using the specified equivalent circuit.

□	Bare Zn			
Degree/°C	35	45	55	65
R_s/Ohm	1.149	1.144	1.201	1.386
Q_{INT}/Fs^{a-1}	6.46E-04	6.74E-04	8.08E-04	1.79E-03
a_{INT}	0.6174	0.6153	0.6119	0.5027
R_{INT}/Ohm	233.6	164.5	104	67.76
	MOF-4@Zn			
Degree/°C	35	45	55	65

R_S/Ohm	1.308	1.22	1.196	1.394
Q_{INT}/Fs^{a-1}	1.31E-03	1.44E-03	2.03E-03	3.03E-03
a_{INT}	0.6429	0.6369	0.6049	0.5673
R_{INT}/Ohm	128.5	91.45	60.26	45.52
	MOF-2@Zn			
Degree/°C	35	45	55	65
R_S/Ohm	1.884	1.609	1.458	1.294
Q_{INT}/Fs^{a-1}	1.00E-03	1.65E-03	2.27E-03	3.58E-03
a_{INT}	0.6531	0.61	0.5855	0.5441
R_{INT}/Ohm	98.5	85.29	63.05	40.68

Electrochemical impedance spectroscopy (EIS) was performed on Zn symmetric cells in a mixed electrolyte of 1 M H_2SO_4 and 1 M $ZnSO_4$ (**Figure S22**). In such strongly acidic conditions, the formation of passivation by-products such as zinc hydroxy sulfate (ZHS) is suppressed. The impedance spectra were quantitatively analyzed using an equivalent circuit consisting of solution resistance (R_S), and interfacial impedance (Z_{INT}), i.e., $Z_{TOTAL} = R_S + Z_{INT}$, where Z_{INT} is modeled as a charge-transfer resistance (R_{INT}) in parallel with a constant phase element (CPE). Here, Rs corresponds to ionic resistance in the bulk electrolyte and R_{INT} reflects the overall kinetics of Zn plating/stripping process. Specifically, the order of electrode with respect to decreasing R_{INT} values is: bare Zn > MOF-4@Zn > MOF-2@Zn across the entire temperature range, demonstrating that MOF-2 most effectively facilitates the interfacial electrochemistry. Furthermore, the Arrhenius analysis of the temperature-dependent R_{INT} further revealed a notable decrease in the activation energy from 36.04 kJ mol^{-1} (bare Zn) to 25.40 kJ mol^{-1} (MOF-2@Zn), confirming that MOF-2 promotes the Zn plating/stripping kinetics.

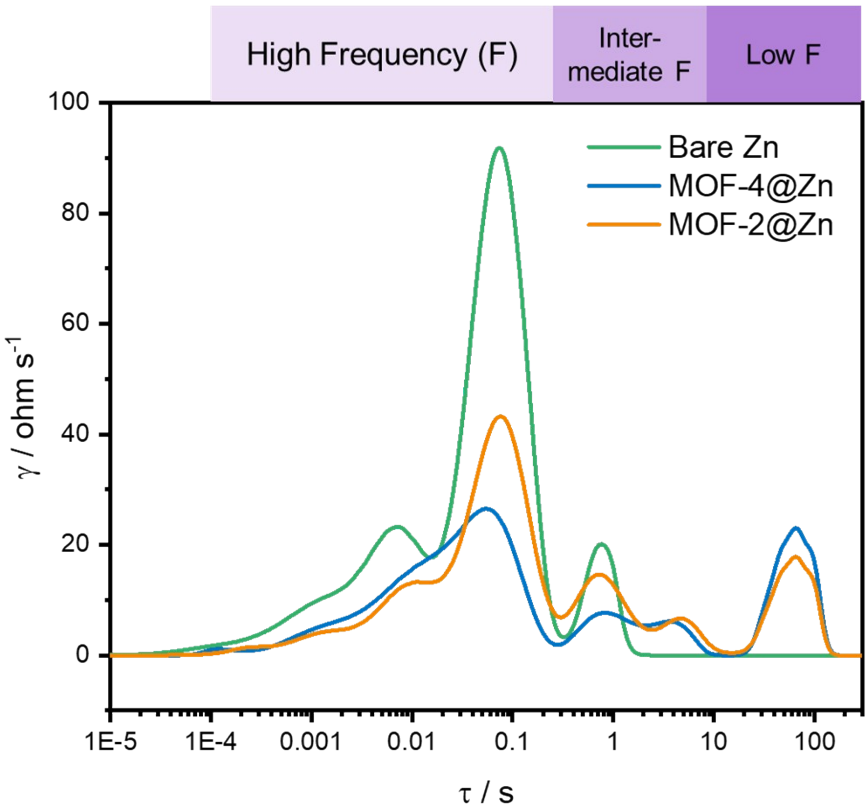

Figure S23. DRT plots of bare Zn, MOF-4@Zn, and MOF-2@Zn at 35 °C.

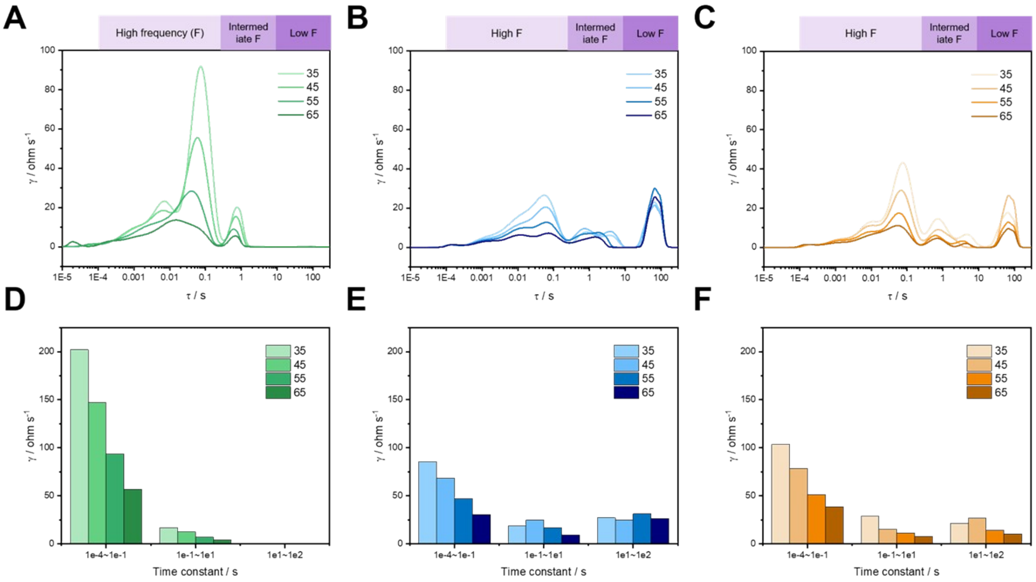

Figure S24. Distribution-of-relaxation-time (DRT) spectra and temperature-dependent resistances in the low-, intermediate-, and high-frequency regimes for (A, D) bare Zn, (B, E) MOF-4@Zn, and (C, F) MOF-2@Zn.

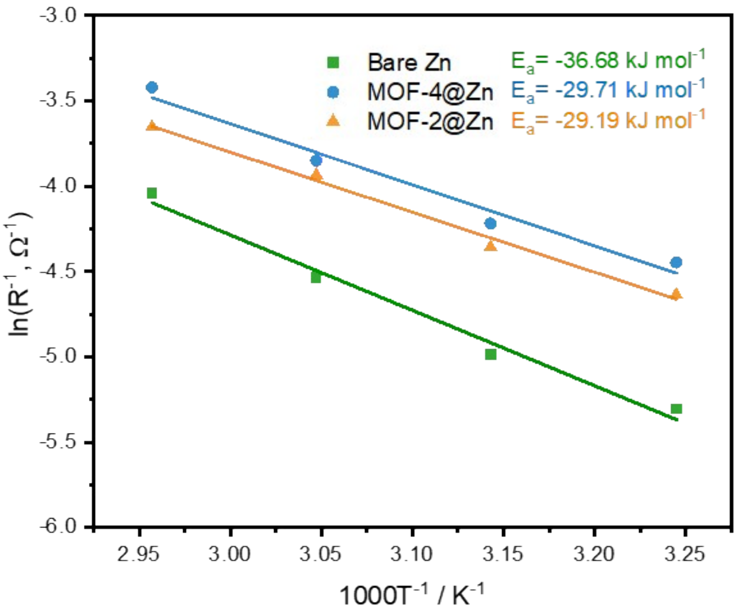

Figure S25. The Arrhenius plot of high frequency regime resistance and the corresponding activation energy.

Table S8. Fitting results of the DRT spectra in Figures S24.

	35		45		55		65	
Bare	τ / s	R / ohm	τ / s	R / ohm	τ / s	R / ohm	τ / s	R / ohm
peak 1	0.75	17	0.7	13	0.61	7.1	0.67	4.1
peak 2	0.074	120	0.061	73	0.042	41	0.022	34
peak 3	0.0072	78	0.0067	74	0.0055	53	0.0019	23
MOF-4@Zn	τ / s	R / ohm	τ / s	R / ohm	τ / s	R / ohm	τ / s	R / ohm
peak 1	0.02	31	0.02	22	0.014	18	0.013	8.1
peak 2	0.068	28	0.071	22	0.072	18	0.076	12
peak 3	0.84	11	0.78	15	0.76	12	0.75	6.2
peak 4	62	27	63	25	68	31	68	26
peak 5	3.6	7.6	3.8	9.4	2.2	4.7	1.8	3.1
peak 6	0.004	26	0.0045	24	0.0019	11	0.0022	11
MOF-2@Zn	τ / s	R / ohm	τ / s	R / ohm	τ / s	R / ohm	τ / s	R / ohm
peak 1	0.012	20	0.012	16	0.014	16	0.018	17
peak 2	0.076	67	0.07	44	0.064	23	0.066	12
peak 3	0.75	20	0.61	7.4	0.65	7.8	0.69	6.1
peak 4	61	22	70	27	66	14	68	10
peak 5	4.5	8.5	1.4	7.6	3.3	3.7	4.3	1.8
peak 6	0.0025	17	0.0029	19	0.0017	13	0.0013	10

To further disentangle the underlying processes masked within the single semicircle, we applied the distribution of relaxation times (DRT) method (**Figures S23-S25**). Each DRT peak corresponds to a distinct RC process, and its peak center represents the time constant (τ) and its integrated area reflects the associated resistance (R), which are summarized in **Table S8** and **Figure S24**. For bare Zn, the response can be separated into three peaks, while MOF-coated electrodes show more complicated spectra due to additional interfacial interactions, leading to multiple partially overlapping peaks. These responses can be grouped into three representative frequency regimes:[30,31]

1. Low frequency (10–100 s): This regime is associated with the slow interfacial relaxation, such as surface adsorption/desorption of H_3O^+ and redistribution of solvated ions. Notably, MOF-coated electrodes exhibit a distinct low-frequency signal absent in bare Zn, which suggests additional relaxation processes arising from ion confinement within the MOF. We attribute this to the trapping of hydronium ions and reorganization of Zn^{2+} solvation shell, which homogenizes the Zn^{2+} transport and suppresses the localized ion accumulation at the interface.
2. Intermediate frequency (10^{-1}–10 s): This regime involves the Zn^{2+} desolvation and the coupled charge-transfer step. Because multiple processes, including partial desolvation, transient H_2O/H_3O^+ interactions, and electron transfer, occur concurrently, the resistance extracted here does not follow a simple Arrhenius relationship and cannot be directly mapped to a single kinetic barrier.
3. High frequency (10^{-4}–10^{-1} s): This regime corresponds to the fast interfacial charging within the inner Helmholtz layer (IHL). Importantly, the high-frequency resistance is the largest among the three regimes under acidic conditions, indicating that it dominates the overall interfacial impedance. Unlike the intermediate and low-frequency regimes, the high-frequency resistance exhibits a clear Arrhenius dependence (**Figure S25**), consistent with a thermally activated

process governed by molecular rearrangements at the electrode/electrolyte interface. The pronounced reduction of this resistance in MOF-coated electrodes strongly suggests that the hydronium trapping in MOF pores probably facilitates the IHL reorganization, consistent with the Tafel analysis (**Figure 4B**), which indicated the reduced proton accessibility at the Zn surface. Notably, MOF-2@Zn exhibits the lowest activation energy in this high-frequency regime, highlighting its trapping ability to accelerate the desolvation and double-layer reconfiguration.

Overall, the additional low-frequency response unique to MOF-coated electrodes emphasizes their role in restructuring the ion solvation and homogenizing the Zn^{2+} transport. Under acidic conditions, the high-frequency regime dominates the interfacial process, implying that the double-layer dynamics—particularly within the inner Helmholtz layer (IHL)—become critical due to the involvement of hydronium and hydrogen species. The pronounced reduction of high-frequency resistance in MOF-coated electrodes further confirms that MOFs reconfigure the IHL via hydronium trapping. These combined effects account for the reduced interfacial resistance and the overall activation energy observed in MOF-coated Zn cells.

4. Morphological and crystallographic analysis

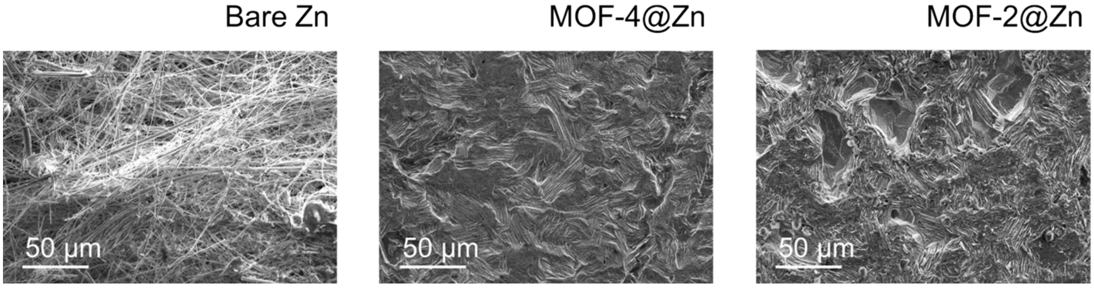

Figure S26. Top-view SEM images of bare Zn, MOF-4@Zn, and MOF-2@Zn electrodes after 50 plating/stripping cycles in symmetric cells operated at 1 mA cm^{-2}/1 mAh cm^{-2}.

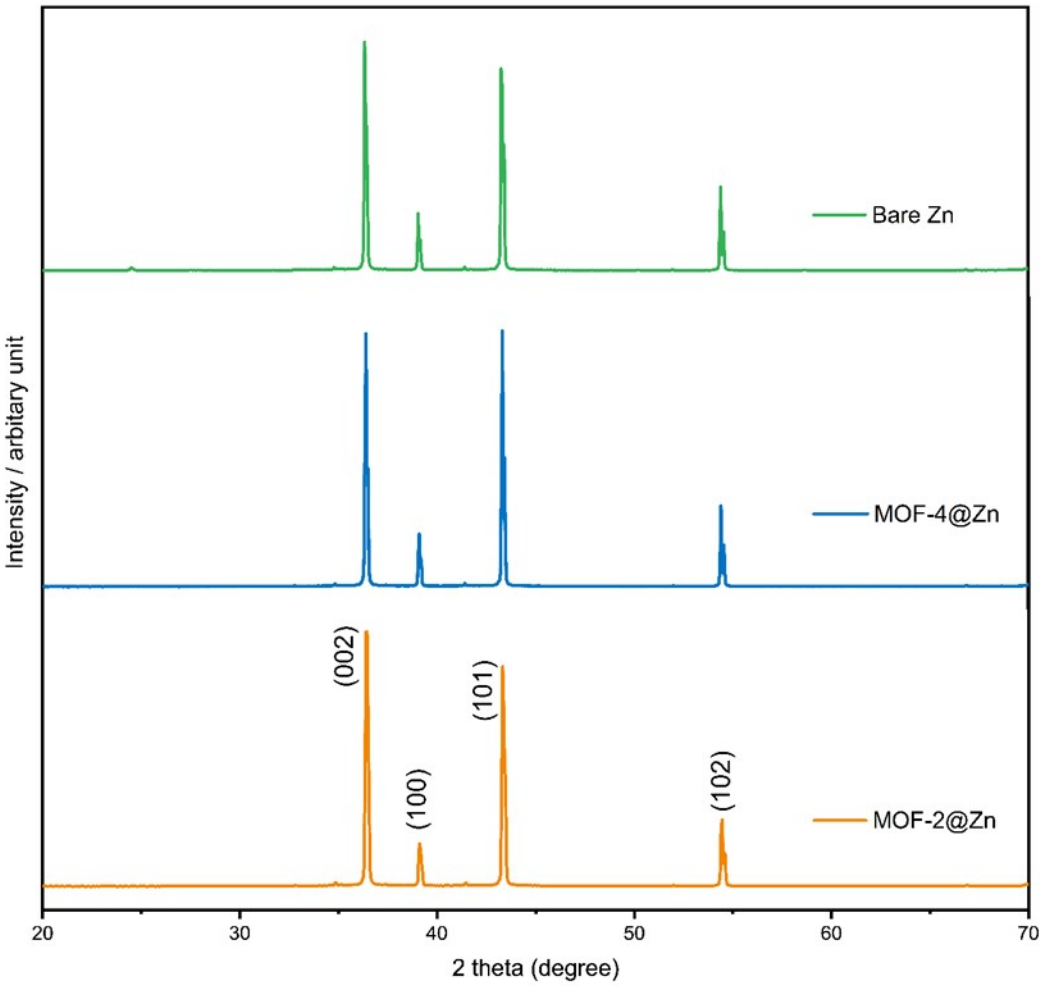

Figure S27. XRD patterns of bare Zn, MOF-4@Zn, and MOF-2@Zn electrodes after 5 cycles in symmetric cells operated at 1 mA cm^{-2}/1 mAh cm^{-2}.

References

1. Prasetya, N., and Li, K. (2022). Synthesis of defective MOF-801 via an environmentally benign approach for diclofenac removal from water streams. Separation and Purification Technology *301*, 122024.
2. Liu, H., Ye, Q., Lei, D., Hou, Z., Hua, W., Huyan, Y., Li, N., Wei, C., Kang, F., and Wang, J.-G. (2023). Molecular brush: an ion-redistributor to homogenize fast Zn 2+ flux and deposition for calendar-life Zn batteries. Energy & Environmental Science *16*, 1610-1619.
3. Cai, X., Tian, W., Zhang, Z., Sun, Y., Yang, L., Mu, H., Lian, C., and Qiu, H. (2024). Polymer Coating with Balanced Coordination Strength and Ion Conductivity for Dendrite-Free Zinc Anode. Advanced Materials *36*, 2307727.
4. Tai, C.-W., Lu, Y.-T., Yi, T.-Y., Liu, Y.-C., Chen, Y.-S., and Hu, C.-C. (2023). A comprehensive study on the interactive effects of carbon crystallinity and electrochemical activation for KOH-modified soft carbons and their high-voltage supercapacitor application. Journal of The Electrochemical Society *170*, 040526.
5. Furukawa, H., Gándara, F., Zhang, Y.-B., Jiang, J., Queen, W.L., Hudson, M.R., and Yaghi, O.M. (2014). Water adsorption in porous metal–organic frameworks and related materials. Journal of the American Chemical Society *136*, 4369-4381.
6. Xu, D., Zhang, H., Xie, J., Zhou, L., Yang, F., Ma, J., Yu, Y., Wang, G., and Lu, X. (2024). Highly reversible tin film anode guided via interfacial coordination effect for high energy aqueous acidic batteries. Advanced Materials *36*, 2408067.
7. Zhang, H., Xu, D., Yang, F., Xie, J., Liu, Q., Liu, D.-J., Zhang, M., Lu, X., and Meng, Y.S. (2023). A high-capacity Sn metal anode for aqueous acidic batteries. Joule *7*, 971-985.
8. Yu, Z., Wang, Q., Li, Y., Zhang, F., Ma, X., Zhang, X., Wang, Y., Huang, J., and Xia, Y. (2024). Highly reversible tin redox chemistry for stable anode-free acidic proton battery. Joule *8*, 1063-1079.
9. Li, X., Tang, Y., Han, C., Wei, Z., Fan, H., Lv, H., Cai, T., Cui, Y., Xing, W., and Yan, Z. (2023). A static tin–manganese battery with 30000-cycle lifespan based on stabilized Mn3+/Mn2+ redox chemistry. ACS nano *17*, 5083-5094.
10. Jiang, H., Shin, W., Ma, L., Hong, J.J., Wei, Z., Liu, Y., Zhang, S., Wu, X., Xu, Y., and Guo, Q. (2020). A high-rate aqueous proton battery delivering power below−78° C via an unfrozen phosphoric acid. Advanced Energy Materials *10*, 2000968.
11. Yue, F., Tie, Z., Deng, S., Wang, S., Yang, M., and Niu, Z. (2021). An ultralow

temperature aqueous battery with proton chemistry. Angewandte Chemie International Edition *60*, 13882-13886.

12. Tong, L., Jing, Y., Gordon, R.G., and Aziz, M.J. (2019). Symmetric all-quinone aqueous battery. ACS Applied Energy Materials *2*, 4016-4021.
13. Zhu, M., Zhao, L., Ran, Q., Zhang, Y., Peng, R., Lu, G., Jia, X., Chao, D., and Wang, C. (2022). Bioinspired catechol-grafting PEDOT cathode for an all-polymer aqueous proton battery with high voltage and outstanding rate capacity. Advanced Science *9*, 2103896.
14. Strietzel, C., Sterby, M., Huang, H., Strømme, M., Emanuelsson, R., and Sjödin, M. (2020). An aqueous conducting redox-polymer-based proton battery that can withstand rapid constant-voltage charging and sub-zero temperatures. Angewandte Chemie International Edition *59*, 9631-9638.
15. Qiao, J., Qin, M., Shen, Y.-M., Cao, J., Chen, Z., and Xu, J. (2021). A rechargeable aqueous proton battery based on a dipyridophenazine anode and an indium hexacyanoferrate cathode. Chemical Communications *57*, 4307-4310.
16. Emanuelsson, R., Sterby, M., Strømme, M., and Sjodin, M. (2017). An all-organic proton battery. Journal of the American Chemical Society *139*, 4828-4834.
17. Guo, Z., Huang, J., Dong, X., Xia, Y., Yan, L., Wang, Z., and Wang, Y. (2020). An organic/inorganic electrode-based hydronium-ion battery. Nature Communications *11*, 959.
18. Sun, T., Du, H., Zheng, S., Shi, J., and Tao, Z. (2021). High power and energy density aqueous proton battery operated at− 90° C. Advanced Functional Materials *31*, 2010127.
19. Yan, L., Huang, J., Guo, Z., Dong, X., Wang, Z., and Wang, Y. (2020). Solid-state proton battery operated at ultralow temperature. ACS Energy Letters *5*, 685-691.
20. Ni, Q., Jiang, H., Sandstrom, S., Bai, Y., Ren, H., Wu, X., Guo, Q., Yu, D., Wu, C., and Ji, X. (2020). A Na3V2 (PO4) 2O1. 6F1. 4 cathode of Zn-ion battery enabled by a water-in-bisalt electrolyte. Advanced Functional Materials *30*, 2003511.
21. Sun, T., Nian, Q., Zheng, S., Shi, J., and Tao, Z. (2020). Layered Ca0. 28MnO2· 0.5 H2O as a high performance cathode for aqueous zinc-ion battery. Small *16*, 2000597.
22. Trócoli, R., and La Mantia, F. (2015). An aqueous zinc-ion battery based on copper hexacyanoferrate. ChemSusChem *8*, 481-485.
23. Lu, Y., Wang, J., Zeng, S., Zhou, L., Xu, W., Zheng, D., Liu, J., Zeng, Y., and Lu, X. (2019). An ultrathin defect-rich Co 3 O 4 nanosheet cathode for high-energy and durable aqueous zinc ion batteries. Journal of Materials Chemistry A *7*,

21678-21683.

24. Zhang, L., Chen, L., Zhou, X., and Liu, Z. (2015). Morphology-dependent electrochemical performance of zinc hexacyanoferrate cathode for zinc-ion battery. Scientific reports *5*, 18263.
25. Ma, L., Chen, S., Li, H., Ruan, Z., Tang, Z., Liu, Z., Wang, Z., Huang, Y., Pei, Z., and Zapien, J.A. (2018). Initiating a mild aqueous electrolyte Co 3 O 4/Zn battery with 2.2 V-high voltage and 5000-cycle lifespan by a Co (iii) rich-electrode. Energy & Environmental Science *11*, 2521-2530.
26. Chao, D., Zhou, W., Ye, C., Zhang, Q., Chen, Y., Gu, L., Davey, K., and Qiao, S.Z. (2019). An electrolytic Zn–MnO2 battery for high-voltage and scalable energy storage. Angewandte Chemie *131*, 7905-7910.
27. Iqbal, M.Z., Zakar, S., and Haider, S.S. (2020). Role of aqueous electrolytes on the performance of electrochemical energy storage device. Journal of Electroanalytical Chemistry *858*, 113793.
28. Rahmanifar, M.S., Hemmati, M., Noori, A., El-Kady, M.F., Mousavi, M.F., and Kaner, R.B. (2019). Asymmetric supercapacitors: An alternative to activated carbon negative electrodes based on earth abundant elements. Materials Today Energy *12*, 26-36.
29. Mendhe, A., and Panda, H. (2023). A review on electrolytes for supercapacitor device. Discover Materials *3*, 29.
30. Yao, Y., Zhao, X., Chang, G., Yang, X., and Chen, B. (2023). Hierarchically porous metal–organic frameworks: synthetic strategies and applications. Small Structures *4*, 2200187.
31. Wang, Y., Wang, T., Mao, Y., Li, Z., Yu, H., Su, M., Ye, K., Cao, D., and Zhu, K. (2024). Reversible protonated electrolyte additive enabling dendrites-free Zn metal anode with high depth of discharge. Advanced Energy Materials *14*, 2400353.